南京航空航天大学

论文集

（二〇一〇年） 第34册

理学院

（第2分册）

南京航空航天大学科技部编

二〇一一年五月

理 学 院

物理

序号	论文作者	学院	论文题目	发表刊名	发表时间
1	李红臣 硕士 阚彩侠 教授 伊兆广 硕士 丁孝龙 硕士 曹艳丽 硕士	082	Synthesis of One Dimensional Gold Nanostructures	Journal of Nanomaterials	2010.962718
2	樊济宇 教授	082	Heisenberg-like ferromagnetism and percolative conductivity in the half-doped manganite	Journal of magnetism and Magnetic Materials	2010,Vol.322
3	樊济宇 教授	082	Critical properties of the perovskite manganite	PHYSICAL REVIEW B	2010,Vol.81
4	樊济宇 教授	082	Invesrigation of charge order manganites $Nd_{0.5}Ca_{0.5}Mn_{0.95}A_{0.025}B_{0.025}O_3$(A=Ti/Ru ;B=Cr/Ga)	physica B	2010,Vol.405
5	樊济宇 教授	082	Magnetocaloric effect of half-doped manganite	physica B	2010,Vol.405
6	牛志平 副教授	082	Spin filter effect and large magnetoresistance in the zigzag graphene nanoribbons	Eur. phys. J. B	2010,Vol.73
7	牛志平 副教授	082	crossed Andreev reflection on a topological insulator	Journal of Applied Physics	2010,Vol.108
8	王田虎 博士 赵志敏 教授	082	Spectroscopic investigations on the binding of dibazol to bovine serum albumin	Journal of Molecular Structure	2010,Vol.970
9	王开圣 工程师 赵力东	082	高速火焰喷涂高质量NiCoCrAlTaReSiY抗氧化涂层	稀有金属材料与工程	2010,Vol.39,No.11
10	王开圣 中级 赵志敏 教授 杨雁南 教授	082	点光源劈尖干涉的条纹分布特征	物理实验	2010,Vol.30,No.1
11	王开圣 中级 赵志敏 教授 刘小廷 副教	082	声速测量实验原理讨论	物理实验	2010,Vol.30,No.3
12	张丽萍 中级	082	Hopf bifurcation in a synaptically coupled fhn neuron model with two delays	Proceedings of the 9 international FLINS conference	2010
13	李红均 博士 赵志敏 教授 朱永刚 俞晓磊	082	Novel model for iteration step selection in image denoising using total variation technique	The Imaging Science Journal	2010,Vol.58
14	朱卫华 博士 赵志敏 教授	082	Study on serum fluorescence soectra based on wavelet transform	African journal of Biotechnology	2010,Vol9(6)
15	张林 博士 赵志敏 教授 金小东 硕士	082	A Novel Measurement System for Dry Rubber Content in Concentrated Latex Based on Y-type Optical Fiber	Journal of Testing and Evalution	2010,Vol.38,No.5
16	李红均 博士 赵志敏 教授 俞晓磊	082	A novel image denoising algorithm in wavelet domain using total variation and grey theory	Engineering Computations	2010,Vol.27,No.7
18	俞晓磊 博士 赵志敏 教授	082	光谱导航技术在果树果实定位中的应用	光谱学与光谱分析	2010,Vol.30,No.3
17	赵志敏 教授 金小东 硕士 张林 博士 俞晓磊 博士	082	A novel measurement system for dry rubber content in concentrated natural latex based on annular photoelectric sensor	International Journal of Physical Sciences	2010,Vol.5(3)

19	赵志敏 教授 洪小芹 李鹏 金小东	082	污染水体中蓝藻叶绿色素的光谱特征分析	光谱学与光谱分析	2010,Vol.30,No.6
20	魏本征 博士 赵志敏 教授	082	An Improved Particle Swarm Optimization Algorithm Based K-means	Journal of information and computational	2010,7,2
21	魏本征 博士 赵志敏 教授	082	A Novel Method of Medical Image Registration Based on Feature Point	Journal of information and computational	2010,7,2
22	魏本征 博士 赵志敏 教授 华普	082	基于改进形态学梯度和Zernike矩的亚像素边缘检测方法	仪器仪表学报	2010,Vol.31,No.4
23	陈远 博士 赵志敏 教授 郑敏 硕士 李洪均 博士	082	人体微小管状血管血液流速自动测量方法研究	计量学报	2010,Vol.31,No.2
24	李洪钧 博士 赵志敏 教授 季雷 博士 张林 博士	082	A Novel Algorithm for Microcirculation Image Enhancement	中国生物医学工程学报（英文版）	2010,Vol.19,No.3
25	宋敏敏 硕士 吴平 教授 董大兴	082	通过噪声等效温差来评价红外系统的性能	红外	2010,Vol.31,No.1
26	张鹏 硕士 吴平 教授 曾辉	082	基于TOD的红外成像系统作用距离研究	红外	2010,Vol.31,No.12
27	吴平 教授	082	物面分波前反射位移调制参考光双曝光全息	中国激光	2010,Vol.37,No.1
28	孙立 高工 李秀 学生	082	基于C++环境下的磁性材料特性测试系统的设计与实现	实验室研究与探索	2010,Vol.29,No.2
29	时阳光 讲师	082	Magnetic and magnetostrictive properties in high-pressure synthesized $DY_{1-x}Pr_xFe_{1.9}$ ($0 \leqslant x \leqslant 1$) cubic Laves alloys	Journal of Alloys Compunds	2010, 506
30	杜朝玲 副高	082	Near-field Coupling Effect Between Individual Au Nanospheres and their	Plasmonics	2010, 5
31	张卫纯 副高	082	Surface-Enhanced Raman Scattering from Different	INEC VOLSLAND	2010, 2
32	张卫纯 副高	082	Surface-enhanced raman scattering from silver nanostructures with different	Appl Phy A	2010, 100
33	王长顺 硕士 阚彩侠 教授 李红臣 研究生	082	Synthesis of High-Yield Gold Nanoplates:Fast Growth Assistant with Binary Surfactants	Journal of Nanomaterials	2010.969030
34	阚彩侠 教授 王长顺 硕士 朱杰君 硕士 李红臣 硕士	082	Formation of gold and silver nanostructures within polyvinylpyrolidone (PVP) gel	Journal of Solid State Chemistry	2010,Vol.183
35	谢翊乐 硕士 王吉明 副教授 刘友文 教授	082	电控振幅型超分辨光瞳滤波器的调谐特性分析	光学学报	2010,Vol.30,No.5
36	阚彩侠 教授 王长顺 硕士 李红臣 齐景山	082	Gold Microplates with Well-Defined Shapes	Small	2010,Vol.6,No.16

37	陈玲玲 硕士 王吉明 副教授 郝崇君 刘友文 教授	082	Electrically Controlled Transverse Superresolution Filter with Axial Focal Shift	Symposium on Photonics and Optoelectronics	2010.978
38	许艳艳 硕士 王东生 副教授 韩东 教授 单伟华	082	基于余热回收的半导体温差发电模型及数值模拟	节能技术	2010,Vol.28,No.160
39	杜建周 硕士 王东生 副教授 谷志刚 学生 赵志敏 教授 陈会 学生 杨世波 学生	082	退火处理对LAA1O3薄膜发光特性的影响	光学学报	2010,Vol.30,No.1
40	王东生 副高 毛万华 谷志刚	082	Study of Digital Silicon Piezoresistive Pressure Sensor with High Precsion	ICISE 2010论文集	2010.12
41	陈红霞 博士 施大宁 教授	082	First-principle study on the structure,electronic,and magneticproperties of Mn-	Physica E	2010,Vol.43
42	朱建伟 博士 施大宁 教授	082	Coupled effects of size and uniaxial force on phase transitions in copper	Nanotechnology	2010,Vol.21
43	陈红霞 博士 施大宁 教授	082	Structure,electronic and magnetic properties of Cr-	PHYSICS LETTERS A	2010,Vol.374
44	邓宇翔 博士 颜晓红 教授 肖扬 副教授 唐娜斯 讲师	082	The circulating in an Aharonov-Bohm ring with a quantum dot:Role of transport current and phonons	Physics Letters A	2010,Vol.374
45	杨玉荣 博士 颜晓红 教授 肖扬 副教授 陆地 讲师	082	Size-dependent strain effects on electronic and optical properties of ZnO nanowires	APPLIED PHYSICS LETTERS	2010,Vol.97
46	马康力 硕士 颜晓红 教授 肖扬 副教授 陈元平	082	Electronic transport properties of metallic graphene nanoribbons with two vacanies	SOLID STATE COMMUNICATIONS	2010,Vol.150
47	张晓禹 硕士 颜晓红 教授 杨玉荣 博士	082	Electronic structure and optical properties of single walled ZnSe nanotubes	Physica E	2010,Vol.42
48	王祥夫 博士 颜晓红 教授 阚彩侠 教授 马康力 硕士 肖扬 副教授 肖思国	082	Enhancement of blue emission in β-$NaYbF_4:Tm^{3+}/Nd^{3+}$ nanophosphors synthesized by nonclosed hydrothermal synthesis method	APPLIED PHYSICS B-LASERS AND OPTICS	2010,Vol.101
49	杨玉荣 博士 颜晓红 教授 沈翔建 博士 张晓禹 硕士 肖杨 副教授	082	Curvature Effects on the Magneism of Ultrashort Zigzag Carbon Nanotubes and Nanographenes	JOURNAL OF PHYSICS CHEMISTRY C	2010,Vol.114
50	郭艳东 博士 颜晓红 教授 肖扬 副教授	082	Spin-polarized current generated by carbon chain and finite nanotube	Journal of Applied Physics	2010,Vol.108

51	曹豆豆 硕士 王开圣 讲师 杨雁南 教授	082	环状激光作用于薄管产生温度场的有限元模拟	激光技术	2010,Vol.34,No.6
52	曹豆豆 硕士 王开圣 讲师 杨雁南 教授	082	激光激发单模兰姆波的有限元模拟	南京航空航天大学学报	2010.8 vol.42 No.4
53	孟云吉 博士 刘友文 教授 朱旻君 李培宁	082	Electro-optic modulation on nonlinear phase shift and fundamental transmission in quasi-phase-matched second-	Optics Comminications	2010,Vol.283
54	李培宁 硕士 刘友文 教授 孟云吉 朱旻君	082	Frequency-tunable superconducting cloaking	J. Phys. D:Appl. Phys	2010,Vol.43
55	李培宁 硕士 刘友文 教授 孟云吉	082	Electrically controlled multifrequency ferroelectric cloak	OPTICS EXPRESS	2010,Vol.18,No.12
56	李培宁 硕士 刘友文 教授 孟云吉 朱旻君	082	A Frequency-tunable cloak with semiconducting constituents	J.Phys.D:Appl.Phys	2010,Vol.43,No.17
57	张广斌 中级 李香莲 副高 李季平 副高	082	各理工科类高校实施大学物理实验课程教学基本要求（2008年版）的必要性	物理与工程	2010,Vol.20,No.3
58	张永梅 副高 邱金斗	082	SPIN INTERFERENCE CAUSED BY SPIN-ORBIT INTERACTION IN NON-MAGNETIC HETEROSTRUCTURES	Modern Physics Letters B	2010,Vol.24,No.17

Hindawi Publishing Corporation
Journal of Nanomaterials
Volume 2010, Article ID 962718, 8 pages
doi:10.1155/2010/962718

Research Article

Synthesis of One Dimensional Gold Nanostructures

Hongchen Li,[1] Caixia Kan,[1] Zhaoguang Yi,[1] Xiaolong Ding,[1] Yanli Cao,[1] and Jiejun Zhu[2]

[1] *College of Science, Nanjing University of Aeronautics and Astronautics, Nanjing 211100, China*
[2] *National Laboratory of Solid State Microstructures and Department of Physics, Nanjing University, Nanjing 210093, China*

Correspondence should be addressed to Caixia Kan, cxkan@nuaa.edu.cn

Received 25 September 2010; Accepted 2 December 2010

Academic Editor: Sherine Obare

Gold nanostructures with shapes of rod, dumbbells, and dog bone have been fabricated by an improved seed-mediated method. It is found that the pH change (the addition of HNO_3 or HCl) and the presence of Ag^+ ions have a great influence on the growth process and aspect ratios of these Au nanocrystals. UV-Vis-NIR absorption spectra for the Au colloidal show that the transverse plasmon absorption band locates at ~520 nm, while the longitudinal plasmon absorption band shifts in a wide spectra region of 750–1100 nm. The obtained Au nanostructures have been investigated by transmission electron microscopy, high-resolution transmission electron microscopy, and X-ray diffractometer. Based on the characterizations and FDTD simulations, most of the obtained Au nanorods are single crystals, possessing an octagonal cross-section bounded by {110} and {100} faces. One model for the anisotropic growth has been proposed. It is found that slow kinetics favor the formation of single-crystalline Au nanorods.

1. Introduction

Noble metallic nanostructures are of great interest due to their unique properties and promising applications in the fields of optics, electronics, magnetism, and catalysis [1–6]. Pt nanoparticles, for instance, were applied as catalyst for the hydrogenation of organic and for selective reactions depending on the crystallographic planes exposed by their surfaces [5, 6]. For the case of optical properties, absorption associated with the collective oscillation of the conduction electrons or surface plasmon resonance (SPR) has been studied for many decades. In recent years, several special shapes and structures have been studied for Au nanoparticles, such as nanorings, nanoplates, dog bones, and nanoprisms. At present, the SPR absorption for arbitrary geometries can be theoretically calculated by discrete dipole approximation or finite difference time domain (FDTD) solutions (FDTD supplies a simple, convenient, and systematic approach to calculate the optical response of a nanostructure with arbitrary symmetry and geometry by solving Maxwell's equations on discrete grids). Both experimental and theoretical studies show that the number and position of the plasmon resonances as well as the spectral range for surface-enhanced Raman scattering (SERS) of metal nanostructures have a strong correlation with their exact morphology and the aspect ratios [1, 7–12]. For example, cylindrical Ag nanowires show one resonance whereas several resonances are expected for Ag nanorods with triangle and other profiles [8, 9]. Two distinctive plasma resonances usually appear in the optical absorption spectra. In addition to a weak transverse surface plasmon resonance (SPR_T) roughly in the visible spectral region (500–530 nm with different solvents), a strong longitudinal surface plasmon resonance (SPR_L) shifts from the visible to the near-infrared (Vis-NIR) region with increasing aspect ratios of Au nanorods [10–12]. This strong polarization sensitivity of SPR absorption in the NIR region is an efficient converter of photon energy to thermal energy, which opens new possibilities for many attractive applied fields. Due to their facile synthesis, ease of functionalization, biocompatibility, and inherent nontoxicity, Au nanoparticles are being developed as ideal biological applications, such as gene delivery, cell imaging, photothermal therapy, and anticancer drug-delivery technology [1, 13–17]. More recently, it is reported five-dimensional (the wavelength, polarization, and 3 spatial dimensions) optical recording mediated by the SPR of Au

nanorods, which allow multiple patterns being stored in the same volume [18]. Under irradiating recording layers doped with Au nanorods of different aspect ratios, the selected nanorods with a certain SPR_L on resonance with the laser light wavelength and polarization would melt. When the readout laser light is implemented, the contrast exhibits.

For fundamental and applied interest, study on the well-controlled shapes and novel structures of Au nanostructures, therefore, has become a very important issue. For one dimensional Au nanorods, different approaches have been demonstrated for synthesizing Au nanorods, including hard templates (such as Al_2O_3 membrane and mesoporous silica) assistant deposition approach [12, 19], electrochemical or photochemical reduction with surfactants [20, 21], and seed-mediated methods [22]. Recently, some groups reported the synthesis of branched and multipod-shaped metal nanostructures with sharp edges and corners [23–27]. Calculation on the fields around nanoparticles show that surface charges are accumulated at the sharp corners that exhibit strong enhancement of an electromagnetic field [28], which makes the nanostructure an excellent candidate as SERS substrates. At the same time, contrast studies on the SPR of these quasi-one-dimensional Au nanostructures demonstrate that the shape and position of the SPR_L was not only sensitive to the aspect ratio but also influenced by additional details of the rod shape and in particular by the natural transition from cylindrical to flared, dog bone, bipyramidal, and dumbbell [29–32].

Here, we report the synthesis of Au nanorods, dumbbells, and dog bone through an improved seed-mediated at room temperature. It is found that the addition of acid, Ag^+ ions and a second surfactant is crucial in both improving the shape and controlling the aspect radios of Au product. A growth model was proposed based on the results.

2. Experimental Section

2.1. Materials. Hydrogen tetrachloroaurate ($HAuCl_4 \cdot 4H_2O$) was purchased from Shanghai Chemical Reagents Company. L-ascorbic acid (AA, 99.7%) and sodium borohydride ($NaBH_4$, 96%) were obtained from Sinopharm Chemical Reagent Company. Cationic cetyltrimethylammonium bromide (CTAB, 99%) and benzyldimethylhexadecyl ammonium chloride (BDAC) were obtained from Nanjing Robiot Company. All other reagents were used without further purification. Deionized water used throughout the experiments was purified by a MilliQ system (18.25 MΩ).

2.2. Synthesis. Seed solutions were generated firstly with a strong reducing agent ($NaBH_4$), followed by preparation of a growth solution with a weaker reducing agent (AA) to grow Au nanorods. In the improved process, chemicals of HNO_3, $AgNO_3$, and BDAC were applied in the growth solution for the understanding of growth mechanism of final product. The details of the process are the following.

2.2.1. Synthesis of Au Seeds. 10 mL CTAB (with molar concentration [CTAB] = 0.1 M) was mixed with 0.05 mL $HAuCl_4$ solution ([$HAuCl_4$] = 0.05 M). Then, 0.6 mL $NaBH_4$ ([$NaBH_4$] = 0.01 M) was injected into the solution under vigorous stirring. The as-obtained seeds are very active indicated by the color change from brownish to red within one day.

2.2.2. Synthesis of Au Dog Bones, Dumbbells, and Nanorods. CTAB was dissolved into10 mL deionized water ([CTAB] = 0.1 M) as growth solution. Then, solutions of 0.2 mL $AgNO_3$ ([$AgNO_3$] = 0.004 M) and 0.1 mL $HAuCl_4$ ([$HAuCl_4$] = 0.05 M) were added to the growth solution. When 0.06 mL AA ([AA] = 0.1 M) was added, the solution color changed from orange to colorless. Finally, 12 μL of the as-prepared seed solution was injected into the growth solution. Under this condition, Au nanostructures with shapes of dog bones and dumbbells were synthesized. In order to fabricate Au nanorods, different amount (0.1 mL, 0.2 mL, 0.3 mL, and 0.4 mL) of acid (HNO_3 or HCl with concentration of 1 M) was employed in the growth solution. When BDAC was used as a cosurfactant, Au nanorods with large aspect ratios were obtained.

2.3. Characterization. The absorption spectra of the prepared samples were collected using a UV-Vis-NIR spectrometer (SP-752PC) in the wavelength range of 200–1100 nm. The products were purified by centrifugation at 14000 rpm for 20 min. Precipitates were centrifugated repeatedly with deionized water. Then, the samples were deposited on copper grids covered by an amorphous carbon film, HRTEM grids, and glass slides for further measurements. Microscopic observations were carried out using transmission electron microscope (TEM: JEOL-100CX) and high-resolution TEM (HRTEM: JEOL-2011). XRD measurement was performed on a diffractometer (Ultima-III, Rigaku).

3. Results and Discussion

3.1. Microstructure and Optical Absorption of Au Nanostructures. As described in the experimental section, Au dog bones and nanorods were prepared, respectively, in the absence and with the presence of HNO_3 with CTAB as surfactant. Figure 1(a) shows the UV-Vis-NIR absorption spectra for the Au colloids of dog bones and nanorods. In contrast to Au nanorods, the SPR_T of dog-bones is wide. Upon addition of HNO_3, the SPR_L position changes from 767 nm to 860 nm, indicating the aspect ratios of Au nanorods increase. It is found that the reduction rate of Au^{3+} ions decreases when acid (HNO_3 or HCl) is added in the growth solution, which facilitates the formation of Au nanorods with large aspect ratios. The structures of the products were characterized by TEM measurements. The SAED patterns indicate the single-crystalline nature of the obtained Au nanocrystals. The dog bone is measured to be 50 nm in average length and 11 nm in diameter for the middle section, and some of the products take the shapes of dumbbell and cube, as exhibited in Figure 1(b). The aspect ratio for Au nanorods in Figure 1(c) is ~4.5. Usually, Au nanorods were available over Au dog bones by

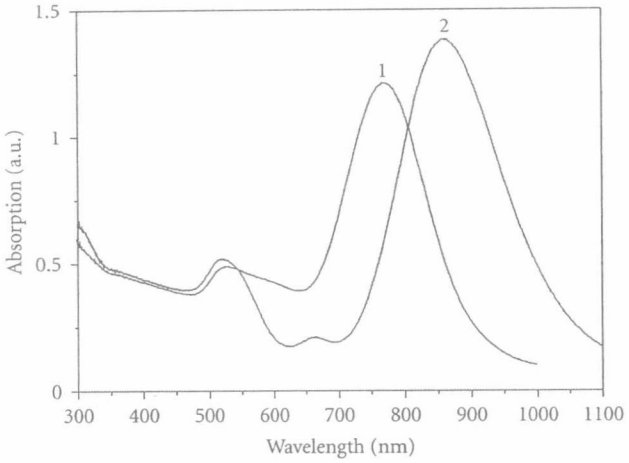

(a)

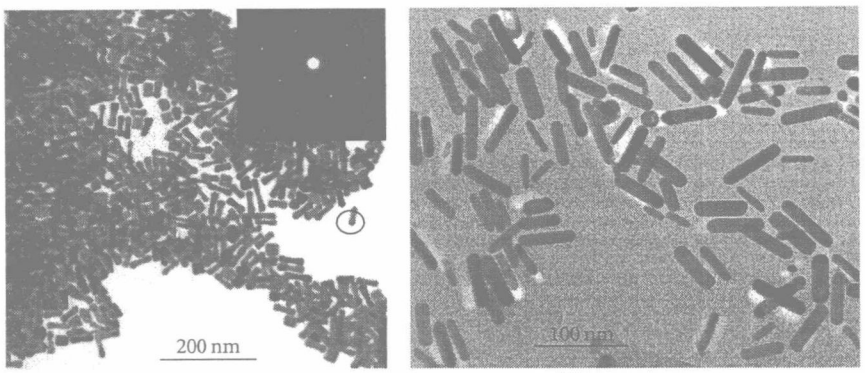

(b) (c)

FIGURE 1: (a) Vis-NIR absorption spectra of Au dog bones (curve-1) and Au nanorods (curve-2) prepared in the absence and with the presence of HNO_3, respectively. (b) and (c) TEM images and SAED pattern of Au dog bones and Au nanorods corresponding to spectra 1 and spectra 2, respectively.

decreasing the content of AA or increasing the content of "seed" solution even in the absence of acid [33, 34]. Instead of these two strategies, it confirms that the addition of HNO_3 is more efficient in modifying the dog bone in our current work. Additionally, the chemical CTAB purchased from different supplies would lead to quite different results; sometimes no Au nanorods were obtained [35]. This could be attributed to the difference of capping ability which significantly influences the morphology of the final products.

To produce Au nanorods with large aspect ratios, a surfactant mixture contained CTAB and BDAC ([BDAC]/[CTAB] = 1.25) was applied in the growth solution. Figure 2(a) shows the UV-Vis-NIR absorption spectra for the colloid of Au nanorods produced with the presence of CTAB/BDAC sampled at different stages. It is clear that the absorption intensity of Au nanostructure increases during aging, suggesting the increase of number and (or) volume of Au nanostructures. The red shift of the SPR_L position indicates that the aspect ratio of Au nanorods increases with time, which is opposite to the reported trend [36]. The recorded spectra also show that Au nanorods maintain their overall shapes during growth process, implying proper rate of Au supply in the colloidal solution. Thus, proper reduction rate favors the formation of nanorods. For the growth of Au dog bones and dumbbells, the formation originates additional deposition of Au cluster at the ends of the as-formed nanorods which could act as seeds.

In our experiments, the presence of HNO_3 or HCl plays an important role in synthesizing Au nanorods. For fully understanding the role of acid, a series of syntheses were performed by altering the content of HNO_3. As shown in Figure 2(b) for samples after addition of seed solution for ~24 h, the SPR_L band blue shifts with increase the content of HNO_3 from 0.1 to 0.4 mL, which offers a useful means to systematically control the shape and aspect ratios of Au nanostructures. Further results show that HNO_3 can slow down the growth rate effectively. For example, the solution became light red after 3 h when 0.2 mL HNO_3 was added, while 5 h was needed for this change with addition of 0.3 mL HNO_3. When HCl was applied, similar results were observed. In the TEM image of Au nanorods, several Au nanocubes were also observed, together with some small nanoparticles as byproducts, as shown in Figure 2(c). The aspect ratio of these nanorods is estimated to be

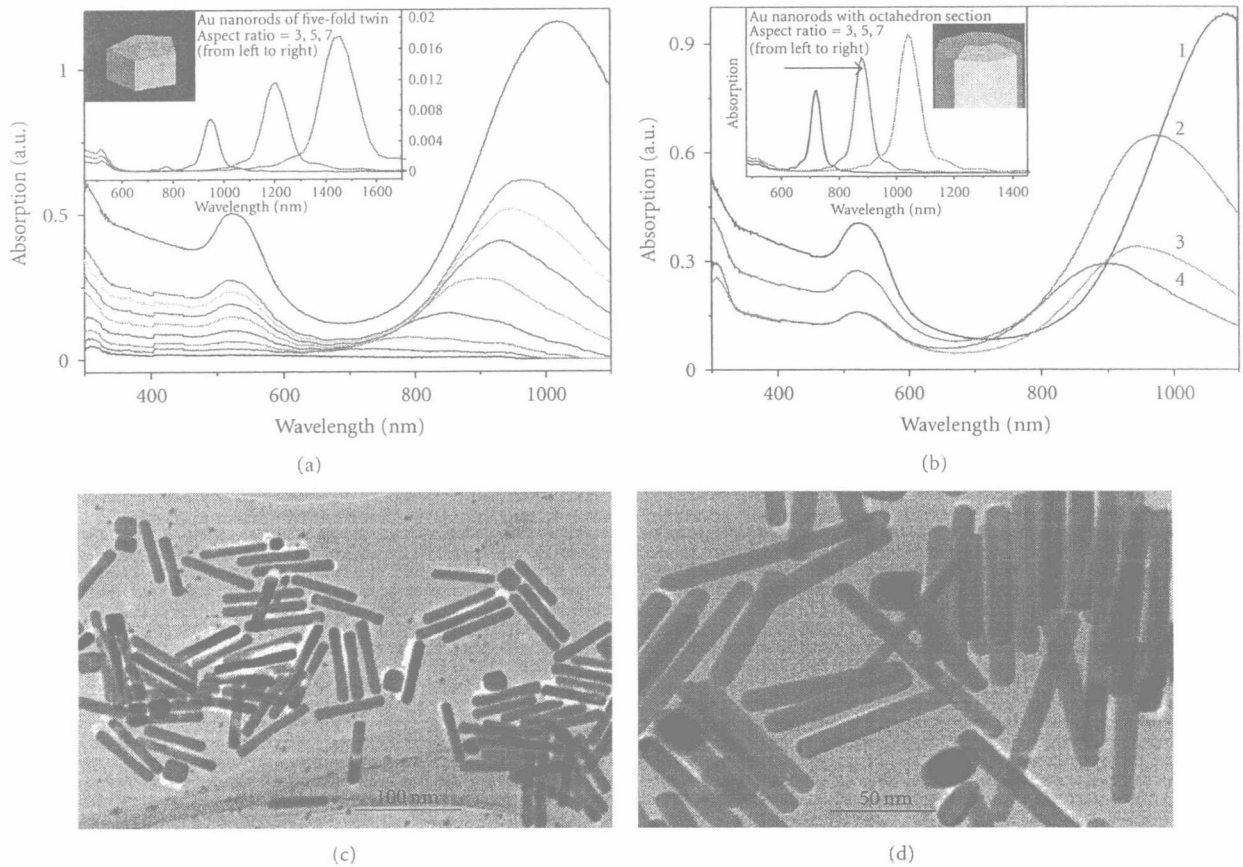

FIGURE 2: (a) Vis-NIR spectra of colloidal Au nanorods aged for various times. Spectra from bottom to top correspond to samples aged for 1–8 hour and 1 day. (b) Vis-NIR spectra of 4 identical growth solutions with increasing HNO_3 (curve-1: 0.1 mL, curve-2: 0.2 mL, curve-3: 0.3 mL, and curve-4: 0.4 mL). Insets of (a) and (b) are the calculated spectra using FDTD solution for Au nanorods with fivefold twin and octahedron cross section (water as medium). TEM images of Au nanorods prepared with HNO_3 (0.1 mL) (c) and HCl (0.2 mL) (d) in a binary surfactants of CTAB and BDAC.

~7 (the average lengths and diameters of nanorods are, resp., ~70 nm and ~10 nm for Figure 2(c) and ~84 nm and ~12 nm for Figure 2(d)), corresponding to the SPR_L band position at 1050 nm. Inserted in Figures 2(a) and 2(b) are the FDTD calculated optical absorption spectra for the fivefold twined Au nanorods and Au nanorods with octahedron cross section (with aspect ratios of 3, 5, and 7, using water as medium). The simulations indicate that the obtained Au nanorods are not five-fold twined crystal, but single-crystalline Au nanorods with octahedron cross section.

Figure 3 shows HRTEM images of representative Au nanorods and dumbbells. The SAED patterns indicate that these structures are single crystals. Au nanorods appear to grow along [001] direction with side faces bounded by {100} and {110} facets. Clear fringes parallel and perpendicular to the growth axis are shown in Figure 3(a). The fringe spacing is 0.200 nm, corresponding well with the lattice spacing of {200} planes for Au crystal (0.203 nm). Similar structures are found for Au dumbbells. Occasionally, the presence of {111} facets were observed at two ends of Au dumbbell, as detailed in Figure 3(b).

To further determine the structure characterization of the Au nanorods, an X-ray diffraction experiment was carried out. Figure 4 shows the typical XRD result of one sample. In the XRD profile, four diffraction peaks can be indexed to fcc Au crystal though the background information is clear due to a very thin layer of Au nanorods covered on the quartz glass substrate. The XRD profile of the Au nanorods shows a strong (111) diffraction peak, and the intensity of the (200) diffraction peak is also strong. The enhanced (111) and (200) diffractions indicate that the stack and elongation of {111} and {100} facets mainly account for the crystals growth.

3.2. Growths of One Dimensional Au Nanocrystals

3.2.1. The Role of Halogen Ions. According to [37], ion addictives, such as NaCl, KCl, and $NaNO_3$, can serve as useful "tools" to tailor the shape, aspect ratio, and yield of Au nanorods. These addictives caused the SPR_L band red shift within the critical concentrations. Ionic strength in colloidal solution has an effect on the size of soft template and suitable ionic concentration can improve micellar structure through reducing the repulsion between the neighboring head group of CTAB [38]. However, further increasing the ionic concentration may prompt a template transfiguration from rod to bone. A series of studies, concentrated on

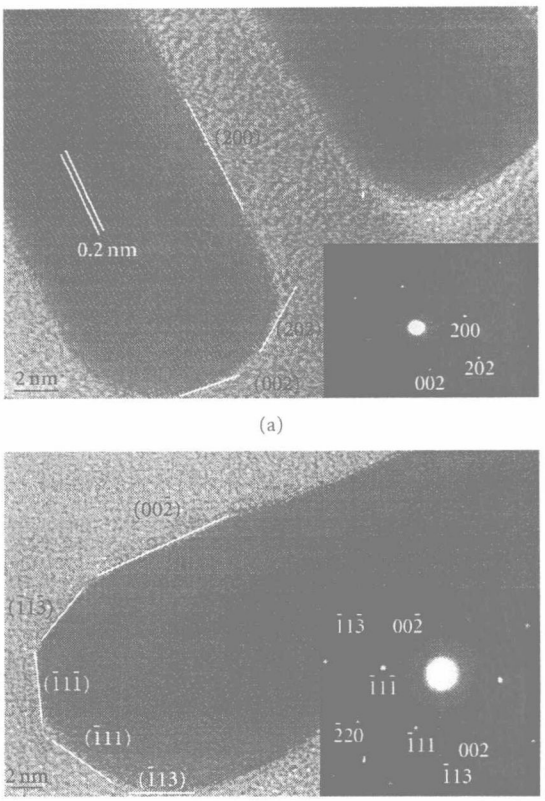

FIGURE 3: (a) HRTEM image of two Au nanorods recorded along [100] direction. The inset shows the corresponding SAED pattern. (b) HRTEM image of one Au dumbbell recorded along [110] direction. The inset shows the corresponding SAED pattern.

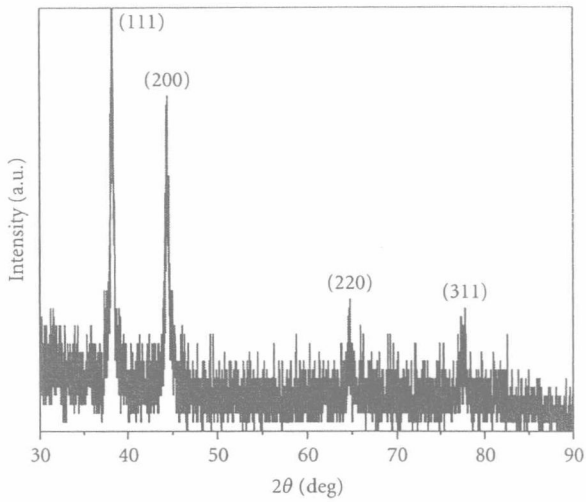

FIGURE 4: X-ray diffraction profile of the as-prepared Au nanorods.

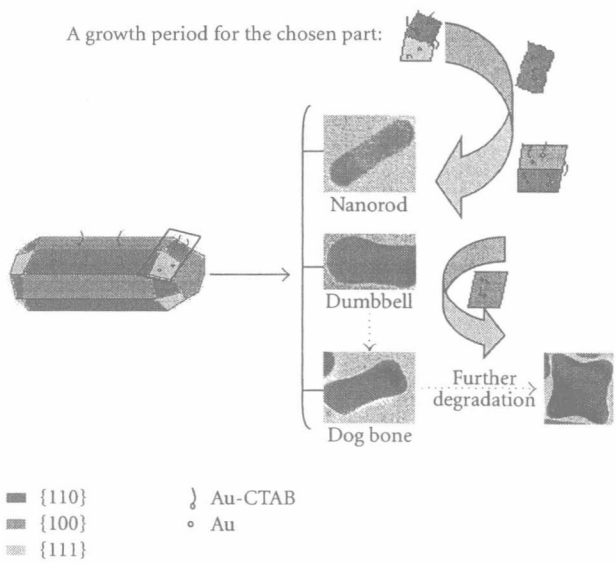

FIGURE 5: Schematic illustration of proposed growth mechanism responsible for the formation of nanorods, dumbbells, and dog bones.

Br^- ions pointed out that Br^- ions aided the formation of structures covered with {110} and {100} facets [39, 40]. We suggest that the major function of halogen is chemisorption on Au crystal surface or chemical interaction between Au crystals and surfactant. Proper concentration of halogen ions avails the formation of single-crystalline Au nanorods with large aspect ratios.

3.2.2. The Role of Ag^+ Ions. Originally, the seed-mediated method without addition of $AgNO_3$ was reported by Jana et al. Au nanorods with high aspect ratio (~18) were obtained for citrate-capped seeds, but the yield was very low [41]. Then, this method was improved to increase the yield of Au nanorods through adding Ag^+ ions to the growth solution [42]. In addition to a high yield of Au nanorods, the SPR_L can be tuned in a wide wavelength range upon increasing the concentration of Ag^+ ions. Based on the soft template of CTAB, AgBr will be formed with addition of $AgNO_3$, which would decrease the charge density of adsorbed CTAB molecules on Au facets and the consequent repulsion between the neighboring head groups, favoring the CTAB template elongation. Another model is that AgBr would adsorb preferentially on special facets and direct the rod-shape growth [33, 39]. Therefore, ideas can be expected for the application of $AgNO_3$. (i) AgBr adsorbs on the single crystalline Au "seed", promoting anisotropic growth into nanorods. (ii) $AgNO_3$ has an effect on making Au nanorods stable and protecting them from evolving into other shapes. Otherwise, when no $AgNO_3$ was introduced, the growth solution turned red within 1 min after the addition of "seed" solution, and the product is dominated by Au nanospheres. In the experiment results, no Ag nanostructures were obtained. This should ascribe to the fact that Ag^+ cannot be reduced in the slightly acidic growth conditions (due to the fact that any $AuCl_4^-$ present is an oxidant with respect to Ag(0)).

3.2.3. The Role of CTAB and BDAC. Undoubtedly, the key factor for prompting the formation of Au nanorods is the

molecules of CTAB. CTAB possesses an ammonium headgroup and a hydrocarbon tail which maybe a driven force for the combination between Au and CTA^+. CTAB forms micelles above its critical micelle concentration. It is widely accepted that CTAB prefer to bind to the side surface of Au nanorods through Br^- ions chemisorbing on the side surfaces [43]. Thus, the side surface is well protected from further deposition. When all conditions remained the same except for the length of the surfactant tail, Au nanorods with high aspect ratios were obtained upon increasing the length of surfactant chain [39, 44]. Others proposed that CTAB micelles acted as a soft template for controlling the shape and size of particles. Au atoms reduced were trapped by the preformed templates, leading to the formation of Au nanorods [37, 38]. In our experiment, solutions of CTAB and CTAB/BDAC were prepared and kept at 10°C. CTAB precipitate was observed in the solution within 30 min, but it took much longer time for the appearance of CTAB precipitate in the mixture solution. This observation demonstrated that the solubility of CTAB is improved dramatically in the CTAB/BDAC mixture solution, and that the templates became more flexible, as evidenced by the elongation of Au nanorods upon aging. Moreover, it is found that the growth of Au nanorods is more time saving in the single-component surfactant than in the binary surfactant mixture.

3.2.4. Growth Model for Different Shapes. For the case of crystal growth in solution phase, the final structure of crystal is determined by both kinetic and thermodynamic effect [9, 45–47]. It is known that thermodynamic control always attempts to minimize the total interfacial free energy of a crystal. However, in the chemical synthesis with the presence of surfactant, the slow reduction rate of Au^{3+} ions provides the possibility for the highly anisotropic growth. The coverage of {110} facets on nanorods seems to deviate from thermodynamic control. This should ascribe to that the surfactant CTAB molecular usually binds to {110} facet with preference, and that the Au atom spacing on the side faces ({110} or {100}) is comparable to the size of the CTA^+ headgroup [39, 48]. Therefore, the single-crystalline Au nanorods have an octagonal cross-section covered by flat {100} facets (the truncated corners are bounded by {111} and {110} facets) with sidewalls of {110} and {100} facets.

In our postulation, the free Au and Au-CTAB complex coexist in the growth solution with different affinity to crystal facets. The Au-CTAB complex are preferred to the {110} facets at the corner of Au rods, while the free Au to the {111} facets. The deposition rate of free Au on {111} facets is faster than that of the bonded Au on {110} facets, which results in the elongation of {110} facets. The growth mechanism of these Au nanostructures can be depicted as schematically illustrated in Figure 5. The {110} facets are not thermodynamically stable and easily evolve into {100} facets with the aid of surfactants, forming the octagonal cross-section covered by both {110} and {100} facets. With increasing the kinetic rate, the rods change from a cylindrical form to a dumbbell and further to dog-bone. A large kinetic rate facilitates the appearance of {100} facets and thus, dog bones dominate the products and then degrade into the cubes.

4. Conclusions

In summary, we conducted the synthesis of single-crystalline Au nanorods, dumbbells, and dog bones in solution phase that contains surfactants with the addition of acid. Through comparing the results, we can see that changes of PH value (by adding HNO_3 and HCl) can modify the morphology and tune the aspect ratios of the final products. The SPR_L of Au nanorods can be tuned in a large spectra range of 750–1100 nm, which is important for the potential applications related to this property. A growth model is proposed, in which kinetics and thermodynamics are employed.

Acknowledgments

This work was financially supported from National Natural Science Foundation of China (Grant nos. 10704038, 10772084, and 51032002). Authors thank Dr. Kai Shen of College of Materials Science of NUAA and Dr. Xiaoguang Zhu of Institute of Solid State Physics of CAS for their great help on HRTEM measurement.

References

[1] K. L. Kelly, E. Coronado, L. L. Zhao, and G. C. Schatz, "The optical properties of metal nanoparticles: the influence of size, shape, and dielectric environment," *Journal of Physical Chemistry B*, vol. 107, no. 3, pp. 668–677, 2003.

[2] B. J. Wiley, Z. Wang, J. Wei, Y. Yin, D. H. Cobden, and Y. Xia, "Synthesis and electrical characterization of silver nanobeams," *Nano Letters*, vol. 6, no. 10, pp. 2273–2278, 2006.

[3] C. B. Murray, S. Sun, H. Doyle, and T. Betley, "Monodisperse 3d Transition-metal (Co, Ni, Fe) nanoparticles and their assembly into nanoparticle superlattices," *MRS Bulletin*, vol. 26, no. 12, pp. 985–991, 2001.

[4] G. A. Somorjai and D. W. Blakely, "Mechanism of catalysis of hydrocarbon reactions by platinum surfaces," *Nature*, vol. 258, no. 5536, pp. 580–583, 1975.

[5] A.-C. Shi and R. I. Masel, "The effects of gas adsorption on particle shapes in supported platinum catalysts," *Journal of Catalysis*, vol. 120, no. 2, pp. 421–431, 1989.

[6] H. Wu, R. Tang, Q. He, X. Liao, and B. Shi, "Highly stable Pt nanoparticle catalyst supported by polyphenol-grafted collagen fiber and its catalytic application in the hydrogenation of olefins," *Journal of Chemical Technology and Biotechnology*, vol. 84, no. 11, pp. 1702–1711, 2009.

[7] J. M. McLellan, Z. Y. Li, A. R. Siekkinen, and Y. Xia, "The SERS activity of a supported ag nanocube strongly depends on its orientation relative to laser polarization," *Nano Letters*, vol. 7, no. 4, pp. 1013–1017, 2007.

[8] P. J. Kottman, O. J. F. Martin, D. R. Smith, and S. Schultz, "Plasmon resonances of silver nanowires with a nonregular cross section," *Physical Review B*, vol. 64, no. 23, Article ID 235402, 10 pages, 2001.

[9] C.-X. Kan, J.-J. Zhu, and X.-G. Zhu, "Silver nanostructures with well-controlled shapes: synthesis, characterization and growth mechanisms," *Journal of Physics D*, vol. 41, no. 15, Article ID 155304, 2008.

[10] J. H. Song, F. Kim, D. Kim, and P. Yang, "Crystal overgrowth on gold nanorods: tuning the shape, facet, aspect ratio, and composition of the nanorods," *Chemistry: A European Journal*, vol. 11, no. 3, pp. 910–916, 2005.

[11] H. Y. Wu, W. L. Huang, and M. H. Huang, "Direct high-yield synthesis of high aspect ratio gold nanorods," *Crystal Growth & Design*, vol. 7, no. 4, pp. 831–835, 2007.

[12] C. Kan, W. Cai, C. Li, G. Fu, and L. Zhang, "Morphologic evolution and optical properties of nanostructured gold based on mesoporous silica," *Journal of Applied Physics*, vol. 96, no. 10, pp. 5727–5734, 2004.

[13] M. Maillard, S. Giorgio, and M. P. Pileni, "Tuning the size of silver nanodisks with similar aspect ratios: synthesis and optical properties," *Journal of Physical Chemistry B*, vol. 107, no. 11, pp. 2466–2470, 2003.

[14] D. A. Stuart, A. J. Haes, C. R. Yonzon, E. M. Hicks, and R. P. Van Duyne, "Biological applications of localised surface plasmonic phenomenae," *IEE Proceedings Nanobiotechnology*, vol. 152, no. 1, pp. 13–32, 2005.

[15] J. Pérez-Juste, I. Pastoriza-Santos, L. M. Liz-Marzán, and P. Mulvaney, "Gold nanorods: synthesis, characterization and applications," *Coordination Chemistry Reviews*, vol. 249, no. 17-18, pp. 1870–1901, 2005.

[16] G. Wu, A. Mikhailovsky, H. A. Khant, C. Fu, W. Chiu, and J. A. Zasadzinski, "Remotely triggered liposome release by near-infrared light absorption via hollow gold nanoshells," *Journal of the American Chemical Society*, vol. 130, no. 26, pp. 8175–8177, 2008.

[17] N. P. Praetorius and T. K. Mandal, "Engineered nanoparticles in cancer therapy," *Recent Patents on Drug Delivery & Formulation*, vol. 1, no. 1, pp. 37–51, 2007.

[18] P. Zijlstra, J. W. M. Chon, and M. Gu, "Five-dimensional optical recording mediated by surface plasmons in gold nanorods," *Nature*, vol. 459, no. 7245, pp. 410–413, 2009.

[19] C. Schönenberger, B. M. I. van der Zande, L. G. J. Fokkink et al., "Template synthesis of nanowires in porous polycarbonate membranes: electrochemistry and morphology," *Journal of Physical Chemistry B*, vol. 101, no. 28, pp. 5497–5505, 1997.

[20] Y. Y. Yu, S. S. Chang, C. L. Lee, and C. R. C. Wang, "Gold nanorods: electrochemical synthesis and optical properties," *Journal of Physical Chemistry B*, vol. 101, no. 34, pp. 6661–6664, 1997.

[21] F. Kim, J. H. Song, and P. Yang, "Photochemical synthesis of gold nanorods," *Journal of the American Chemical Society*, vol. 124, no. 48, pp. 14316–14317, 2002.

[22] N. R. Jana, L. Gearheart, and C. J. Murphy, "Wet chemical synthesis of silver nanorods and nanowires of controllable aspect ratio," *Chemical Communications*, no. 7, pp. 617–618, 2001.

[23] N. Zettsu, J. M. McLellan, B. Wiley, Y. Yin, Z. Y. Li, and Y. Xia, "Synthesis, stability, and surface plasmonic properties of rhodium multipods, and their use as substrates for surface-enhanced raman scattering," *Angewandte Chemie International Edition*, vol. 45, no. 8, pp. 1288–1292, 2006.

[24] Z. Li, W. Li, P. H. C. Camargo, and Y. Xia, "Facile synthesis of branched Au nanostructures by templating against a self-destructive lattice of magnetic Fe nanoparticles," *Angewandte Chemie International Edition*, vol. 47, no. 50, pp. 9653–9656, 2008.

[25] T. K. Sau and A. L. Rogach, "Nonspherical noble metal nanoparticles: colloid-chemical synthesis and morphology control," *Advanced Materials*, vol. 22, no. 16, pp. 1781–1804, 2010.

[26] I. I. Naumov, Z. Li, and A. M. Bratkovsky, "Plasmonic resonances and hot spots in Ag octopods," *Applied Physics Letters*, vol. 96, no. 3, Article ID 033105, 2010.

[27] M. J. Mulvihill, X. Y. Ling, J. Henzie, and P. Yang, "Anisotropic etching of silver nanoparticles for plasmonic structures capable of single-particle SERS," *Journal of the American Chemical Society*, vol. 132, no. 1, pp. 268–274, 2010.

[28] E. Hao, G. C. Schatz, and J. T. Hupp, "Synthesis and optical properties of anisotropic metal nanoparticles," *Journal of Fluorescence*, vol. 14, no. 4, pp. 331–341, 2004.

[29] T. K. Sau and C. J. Murphy, "Role of ions in the colloidal synthesis of gold nanowires," *Philosophical Magazine*, vol. 87, no. 14-15, pp. 2143–2158, 2007.

[30] X. Liu, R. Huang, and J. Zhu, "Functional faceted silver nanohexapods: synthesis, structure characterizations, and optical properties," *Chemistry of Materials*, vol. 20, no. 1, pp. 192–197, 2008.

[31] K. Park and R. A. Vaia, "Synthesis of complex Au/Ag nanorods by controlled overgrowth," *Advanced Materials*, vol. 20, no. 20, pp. 3882–3886, 2008.

[32] C. Li, K. L. Shuford, Q. H. Park et al., "High-yield synthesis of single-crystalline gold nano-octahedra," *Angewandte Chemie International Edition*, vol. 46, no. 18, pp. 3264–3268, 2007.

[33] T. K. Sau and C. J. Murphy, "Seeded high yield synthesis of short Au nanorods in aqueous solution," *Langmuir*, vol. 20, no. 15, pp. 6414–6420, 2004.

[34] L. Gou and C. J. Murphy, "Fine-tuning the shape of gold nanorods," *Chemistry of Materials*, vol. 17, no. 14, pp. 3668–3672, 2005.

[35] D. K. Smith and B. A. Korgel, "The importance of the CTAB surfactant on the colloidal seed-mediated synthesis of gold nanorods," *Langmuir*, vol. 24, no. 3, pp. 644–649, 2008.

[36] X. Xu and M. B. Cortie, "Shape change and color gamut in gold nanorods, dumbbells, and dog bones," *Advanced Functional Materials*, vol. 16, no. 16, pp. 2170–2176, 2006.

[37] K. T. Yong, Y. Sahoo, M. T. Swihart, P. M. Schneeberger, and P. N. Prasad, "Templated synthesis of gold nanorods (NRs): the effects of cosurfactants and electrolytes on the shape and optical properties," *Topics in Catalysis*, vol. 47, no. 1-2, pp. 49–60, 2008.

[38] B. Nikoobakht and M. A. El-Sayed, "Preparation and growth mechanism of gold nanorods (NRs) using seed-mediated growth method," *Chemistry of Materials*, vol. 15, no. 10, pp. 1957–1962, 2003.

[39] C. J. Murphy, T. K. Sau, A. M. Gole et al., "Anisotropic metal nanoparticles: synthesis, assembly, and optical applications," *Journal of Physical Chemistry B*, vol. 109, no. 29, pp. 13857–13870, 2005.

[40] Y. Xiong, H. Cai, B. J. Wiley, J. Wang, M. J. Kim, and Y. Xia, "Synthesis and mechanistic study of palladium nanobars and nanorods," *Journal of the American Chemical Society*, vol. 129, no. 12, pp. 3665–3675, 2007.

[41] N. R. Jana, L. Gearheart, and C. J. Murphy, "Wet chemical synthesis of high aspect ratio cylindrical gold nanorods," *Journal of Physical Chemistry B*, vol. 105, no. 19, pp. 4065–4067, 2001.

[42] N. R. Jana, L. Gearheart, and C. J. Murphy, "Seed-mediated growth approach for shape-controlled synthesis of spheroidal and rod-like gold nanoparticles using a surfactant template," *Advanced Materials*, vol. 13, no. 18, pp. 1389–1393, 2001.

[43] C. J. Murphy, A. M. Gole, S. E. Hunyadi, and C. J. Orendorff, "One-dimensional colloidal gold and silver nanostructures," *Inorganic Chemistry*, vol. 45, no. 19, pp. 7544–7554, 2006.

[44] J. Gao, C. M. Bender, and C. J. Murphy, "Dependence of the gold nanorod aspect ratio on the nature of the directing surfactant in aqueous solution," *Langmuir*, vol. 19, no. 21, pp. 9065–9070, 2003.

[45] C. Kan, X. Zhu, and G. Wang, "Single-crystalline gold microplates: synthesis, characterization, and thermal stability," *Journal of Physical Chemistry B*, vol. 110, no. 10, pp. 4651–4656, 2006.

[46] C. Kan, C. Wang, J. Zhu, and H. Li, "Formation of gold and silver nanostructures within polyvinylpyrollidone (PVP) gel," *Journal of Solid State Chemistry*, vol. 183, no. 4, pp. 858–865, 2010.

[47] C. Kan, C. Wang, H. Li et al., "Gold microplates with well-defined shapes," *Small*, vol. 6, no. 16, pp. 1768–1775, 2010.

[48] Z. L. Wang, R. P. Gao, B. Nikoobakht, and M. A. El-Sayed, "Surface reconstruction of the unstable {110} surface in gold nanorods," *Journal of Physical Chemistry B*, vol. 104, no. 23, pp. 5417–5420, 2000.

Journal of Magnetism and Magnetic Materials 322 (2010) 3692–3695

Contents lists available at ScienceDirect

Journal of Magnetism and Magnetic Materials

journal homepage: www.elsevier.com/locate/jmmm

Heisenberg-like ferromagnetism and percolative conductivity in the half-doped manganite $Nd_{0.5}Ca_{0.25}Sr_{0.25}MnO_3$

Jiyu Fan [a,*], Bo Hong [b], Lei Zhang [c], Yangguang Shi [a], Wei Tong [c], Langsheng Ling [c], Li Pi [d], Yuheng Zhang [c,d]

[a] Department of Applied Physics, Nanjing University of Aeronautics and Astronautics, Nanjing 210016, China
[b] Department of Material Engineering, China Jiliang University, Hangzhou 310018, China
[c] High Magnetic Field Laboratory, Chinese Academy of Sciences, Hefei 230031, China
[d] Hefei National Laboratory for Physical Sciences at the Microscale, University of Science and Technology of China, Hefei 230026, China

ARTICLE INFO

Article history:
Received 25 March 2010
Received in revised form
4 June 2010
Available online 23 July 2010

Keywords:
Critical phenomena
Eletrical transport
Manganites

ABSTRACT

The magnetic behavior and electronic transport in the half-doped manganite $Nd_{0.5}Ca_{0.25}Sr_{0.25}MnO_3$ have been investigated. The critical exponents are studied by using isothermal magnetization methods. The results show that the paramagnetic–ferromagnetic transition is second order and the magnetic interaction is satisfied with the prediction of three-dimensional Heisenberg model. The electronic transport belongs to the percolation mechanism. These findings demonstrate that the critical behavior of the magnetic transition and conductivity for manganites are related to Mn-site ordering degree.

1. Introduction

Perovskite manganites $R_{1-x}A_xMnO_3$ (R=trivalent rare earth, A=divalent alkaline earth) show a great variety of fascinating properties such as colossal magnetoresistance (CMR) effect and electronic phase separation [1–4]. It has been extensively accepted that the double exchange (DE) effect in which e_g electrons hop between Mn^{3+} and Mn^{4+} visa oxygen ions with a strong on-site Hunds-rule coupling is essential for understanding the magnetic and transport properties in manganites [5]. However, if the DE effect is solely considered, the calculated resistivity obviously deviated from the experimental observations [6,7]. Then, a electron–phonon coupling was included due to Jahn–Teller lattice distortion [8,9].

Besides CMR effect, another intriguing phenomenon of charge ordering (CO) phase has been frequently observed in manganite. As we know, for the half-doped manganites $R_{0.5}A_{0.5}MnO_3$, the CO phase reveals a periodic arrangement of Mn^{3+} and Mn^{4+} ions. Usually, the CO state can be kept stably in manganites, except for some extreme exoteric perturbations. For example, Tokunaga et al. [10] found that the CO state still remained stable even under magnetic fields up to 27 T in $Pr(Nd)_{0.5}Ca_{0.5}MnO_3$. In addition to the external field, quenched disorder arising from the local lattice distortion and/or doped impurities can significantly modify CO state. A few percent substitutions of Cr easily destroy the long-range CO phase and induce the ferromagnetic phase locally, which results in the phase separated ground state with both CO and FM clusters randomly distributed [11–13]. However, our recent research shows that the paramagnetism–ferromagnetism (PM–FM) transition and insulator–metal (IM) transition are observed in the half-doped manganite $Nd_{0.5}Sr_{0.25}Ca_{0.25}MnO_3$ [14]. Due to the large mismatch of ionic size between Ca^{2+} and Sr^{2+} (r_{Ca}=1.18 Å, r_{Sr}=1.31 Å), a considerable disorder on A-site causes inhomogeneous strain field so that it is impossible to form a long-rang CO phase. However, for the reason of PM–FM phase transition and IM transition, it is not very clear in the present system. In this paper, we measured the static magnetization around Curie temperature (T_C) and investigated the critical properties. The obtained critical exponents are close to that predicted by a three-dimensional (3D) Heisenberg model. It suggests that the observed ferromagnetism is short-range magnetic interaction.

2. Experiment

Polycrystalline sample $Nd_{0.5}Ca_{0.25}Sr_{0.25}MnO_3$ was synthesized by the conventional solid-state reaction method with high pure Nd_2O_3, $SrCO_3$, $CaCO_3$, MnO_2. The detailed experimental process has been reported in Ref. [14]. The Powder X-ray diffraction was employed on Japan Rigaku D/max-$\gamma\alpha$ rotating powder diffractometer using Cu Kα radiation to check the structure and phase purity. The samples were proved to be single-phase orthorhombic

* Corresponding author.
E-mail address: fanjiyu@gmail.com (J. Fan).

0304-8853/$ - see front matter Crown Copyright © 2010 Published by Elsevier B.V. All rights reserved.
doi:10.1016/j.jmmm.2010.07.027

structure. The resistivity (ρ) was measured by standard four-probe method. The magnetization (M) measurement was performed using the Quantum Design Superconducting Quantum Interference Device under 0.01 T magnetic field in the range of 5–300 K. The $M(H)$ curve was measured with sweep field from 0 to 3.0 T. Moreover, in order to ensure a perfect demagnetization of the samples, each measurement was performed only after the sample was heated firstly above T_C.

3. Results and discussion

Fig. 1(a) shows the temperature dependence of magnetization and resistance for $Nd_{0.5}Ca_{0.25}Sr_{0.25}MnO_3$ sample. The conductivity of $Nd_{0.5}Ca_{0.25}Sr_{0.25}MnO_3$ displays an IM transition at $T_{Im}=175$ K. Correspondingly, a PM–FM transition occurs at the same temperature. Generally, as for the half-doped manganites, the charge ordering state and antiferromagnetic phase are ubiquitous. However, in the present materials, these characters have not been observed. In our previous investigation [14], we have suggested that the A-site cation disorder induced by the size mismatch between Sr^{2+} ion and Ca^{2+} ion was mainly responsible for this phenomenon. However, for further understanding the above behavior, two important questions about PM–FM transition should be firstly considered: one is the order of phase transition, the other is the common universality class. To make these issues clear, we investigated the critical exponents around the region of the PM–FM transition based on the measurement of isothermal magnetization as shown in Fig. 1(b).

As we known, the thermodynamic function around the critical point can be expressed by a power law form. According to the scaling hypothesis [15,16], a second-order magnetic phase transition near Curie point is characterized by a set of critical exponents, β (associated with the spontaneous magnetization M_s), γ (associated with the initial magnetic susceptibility χ_0), δ (associated with the critical magnetization isotherm at T_C). The mathematical definitions of the exponents from magnetization measurements are given below:

$$M_S(T)=M_0(-\varepsilon)^{\beta}, \quad \varepsilon<0,\ T<T_C \tag{1}$$

$$\chi_0^{-1}(T)=(h_0/M_0)\varepsilon^{\gamma}, \quad \varepsilon>0,\ T>T_C \tag{2}$$

$$M=DH^{1/\delta}, \quad \varepsilon=0,\ T=T_C \tag{3}$$

where ε is the reduced temperature $(T-T_C)/T_C$, and M_0, h_0/M_0, and D are the critical amplitudes.

In addition, near the critical point of a second-order transition, the free energy G can be expressed in terms of the order parameter M in the following form:

$$G(T,M)=G_0+aM^2+bM^4-MH \tag{4}$$

where the coefficients of a and b are temperature-dependent parameters. For the condition of equilibrium, i.e., energy minimization, $\partial G/\partial M=0$, the magnetic equation of state is obtained as

$$H/M=2a+4bM^2 \tag{5}$$

Thus, the relationship of M^2 vs. H/M should be shown as a linear behavior around T_C. According to the criterion proposed by Banerjee [17], the order of magnetic transition can be determined from the slope of straight line. The positive slope corresponds to the second-order transition while the negative slope corresponds to the first-order transition. Fig. 2(a) is an Arrott plot of M^2 vs. H/M. Clearly, in the present case the positive slope of M^2 vs. H/M curves indicates the phase transition is a second-order PM–FM phase transition. However, all the curves in the Arrott plot are nonlinear and shows upward curvature even at high field indicating the critical exponent of $\beta=0.5$ and $\gamma=1.0$ is not satisfied according to Arrott–Noakes equation of state $(H/M)^{1/\gamma}=(T-T_C)/T_C+(M/M_1)^{1/\beta}$ [18]. Namely, the mean-field theory [16,19], which exponent is of $\beta=0.5$ and $\gamma=1.0$, cannot be used to describe the critical behavior in present $Nd_{0.5}Ca_{0.25}Sr_{0.25}MnO_3$ system.

In order to determine the critical exponents accurately, a modified Arrott plot with Arrott–Noakes equation is used. As the critical exponents β and γ are correctly chosen, the modified Arrott plot will produce a set of parallel straight lines. Using a polynomial fit with Eq. (5) and extrapolating the data in Fig. 2(a), the intercepts of the isotherms on the H/M and M^2 axes give the values of $\chi_0^{-1}(T)$ for $T>T_C$ and $M_S(0,T)$ for $T<T_C$, respectively. Thus, one can plot the $M_S(0,T)$ vs. T and $\chi_0^{-1}(T)$ vs. T curves, as shown in set of Fig. 2(b). Then, using Eqs. (1) and (2), the fitting results produce two new critical exponents β and γ. These two new values of β and γ are used to make the Arrott plot. The procedure is performed repeatedly until the values of β and γ do not change. Finally, the modified Arrott plot is shown in Fig. 2(b). With the final value of $\beta=0.386(2)$ and $\gamma=1.174(4)$, one can obtain a set of parallel lines around critical region. The obtained critical exponents are close to theoretically predicted values of 3D-Heisenberg magnets ($\beta=0.365$ and $\gamma=1.336$) [20,21]. Alternatively, the critical exponents can be obtained from the

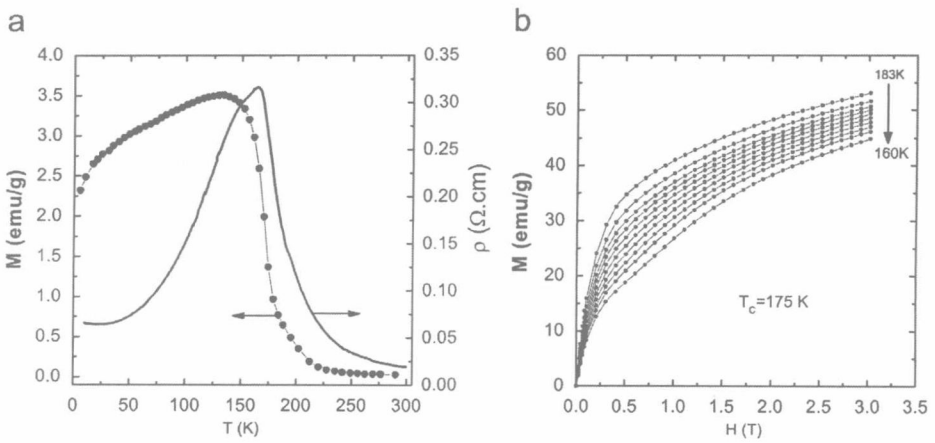

Fig. 1. (a) Magnetization vs. temperature and resistivity vs. temperature of $Nd_{0.5}Ca_{0.25}Sr_{0.25}MnO_3$; (b) magnetization vs. magnetic field at different temperatures around the Curie temperature ($T_C=175$ K).

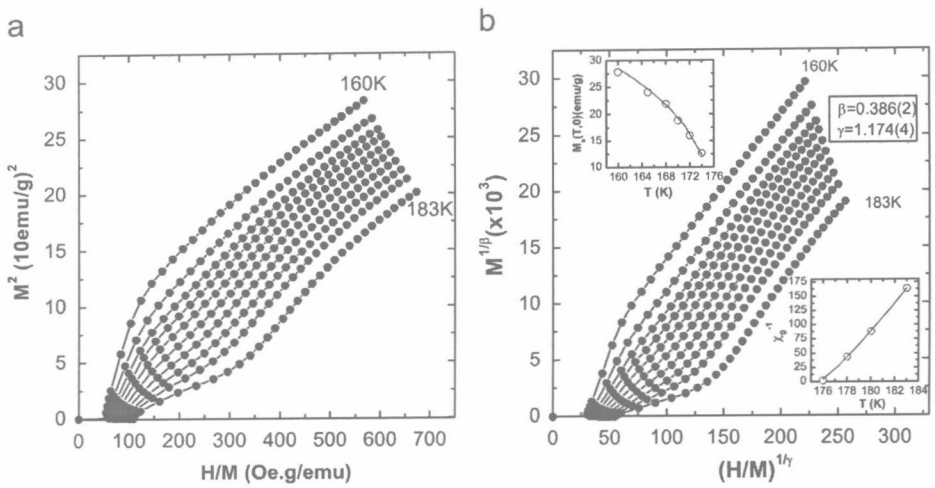

Fig. 2. (a) Isotherms of H/M vs. M^2 of $Nd_{0.5}Ca_{0.25}Sr_{0.25}MnO_3$ at different temperatures around the Curie temperature (T_C=175 K); (b) modified Arrott plot of $M^{1/\beta}$ vs. $(H/M)^{1/\gamma}$ with: $\beta=0.386$ and $\gamma=1.174$; the inset is the temperature as a function of the spontaneous magnetization $M_s(T,0)$ (open circles) and the inverse initial susceptibility $\chi_0^{-1}(T)$ (open circles) along with the fitting curves based on the power laws (solid lines).

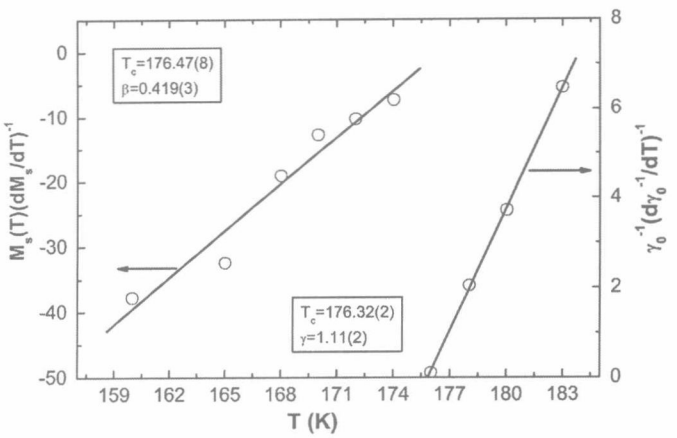

Fig. 3. Kouvel–Fisher plots for the spontaneous magnetization M_s (left) and the inverse initial susceptibility χ_0^{-1} (right).

Kouvel–Fisher (KF) method as well [22]:

$$\frac{M_s(T)}{dM_s(T)/dT}=\frac{T-T_C}{\beta} \tag{6}$$

$$\frac{\chi_0^{-1}(T)}{d\chi_0^{-1}(T)/dT}=\frac{T-T_C}{\gamma} \tag{7}$$

According to this method, $M_s(dM_s/dT)^{-1}$ vs. T and $\chi_0^{-1}(d\chi_0^{-1}/dT)^{-1}$ vs. T should yield straight lines with slopes $1/\beta$ and $1/\gamma$, respectively. When these straight lines are extrapolated to the ordinate equal to zero, the intercepts on T axis just correspond to T_C. As presented in Fig. 3, the fitting results with KF method give the exponents and T_C to be of $\beta=0.419(3)$ with T_C=176.47(8) K and $\gamma=1.11(2)$ with T_C=176.32(2) K. Obviously, the obtained values of the critical exponents and T_C using the KF method are in agreement with that using the modified Arrott plot of 3D-Heisenberg model. The value of δ was obtained by plotting the critical isotherm. The inset of Fig. 4 shows the M vs. H plot on a log scale for the $M(H)$ curve at T=176 K. According to Eq. (3), the data of the high-field region can be fitted by a straight line with slop of $1/\delta$. This gives the value of $\delta=2.71(6)$.

Here, the obtained critical values can be compared with the prediction of the scaling theory. In the critical region, the magnetic equation can be written as

$$M(H,\varepsilon)\varepsilon^{-\beta}=f_{\pm}(H/\varepsilon^{\beta+\gamma}) \tag{8}$$

where f_+ for $T>T_C$ and f_- for $T<T_C$ are regular functions [23]. Eq. (8) indicates that $M\varepsilon^{-\beta}$ as a function of $H\varepsilon^{-(\beta+\gamma)}$ yields two universal curves: one for temperature $T>T_C$ and the other for temperature $T<T_C$. As shown in Fig. 5, the experimental data fall on two curves, one above T_C and the other below T_C, in agreement with the scaling theory of Eq. (8). This result indicates that the obtain values of the critical exponents and T_C are reliable. Moreover, the characterization of the critical properties with the 3D-Heisenberg model is appropriate in the present system.

Based on the results above, we can understand the PM–FM and IM transition from the following scenario. In the present $Nd_{0.5}Ca_{0.25}Sr_{0.25}MnO_3$ system, even though it is a half-doped manganite with the ratio Mn^{3+}:$Mn^{4+}=1$, CO characteristic is not observed. On the contrary, its behavior is similar to that in the ferromagnetic manganites $R_{0.7}A_{0.3}MnO_3$ [24,25]. Due to the size mismatch between Sr^{2+} ion and Ca^{2+} ion, the quenched disorder causes Sr^{2+} ions congregate some regions while Ca^{2+} ions accumulate in other ones. In the former region, it prefers to form the FM coupling which produce a short-range PM–FM phase transition as the decrease of temperature, but in the Ca^{2+} rich region, it tends to suppress the Mn^{3+}–Mn^{4+} DE and form CO-antiferromagnetic (AFM) phase. Therefore, it is nature to form the short-range FM interaction and the local CO-AFM phase. In fact, from Fig. 1(a), one can find the magnetization exhibits a noticeable decrease below T_C. Moreover, in Fig. 1(b) and in our previous research, the magnetization cannot reach saturation around T_C under 3 T magnetic field or at 5 K under 6 T magnetic field. It implied that the local AFM phase occurs at $T<T_C$. The coexistence and competition between FM and CO-AFM phase induces a spin glass state at low temperatures. According to 3D-Heisenberg model, the isotropic magnetic coupling belong to short-range FM exchange interaction. Correspondingly, the electronic transport should show an insulting behavior. However, as shown in Fig. 1(a), the conductivity displays an IM transition. We suggest that these phenomena can be understood by the percolation model. With temperature decreasing, the thermal fluctuation is weakened and the coupling between the short-range FM phases is increased. The increasing FM component forms a percolation channel around T_C. As it reaches the percolation threshold, the electronic transport reveals an IM transition even though the insulting CO-AFM phases are random